# Evolution of CIR storm on 22 July 2009

J. D. Perez,[1] E. W. Grimes,[1] J. Goldstein,[2,3] D. J. McComas,[2,3] P. Valek,[2,3] and N. Billor[4]

[1]   Global images of ion intensities are deconvolved from TWINS ENA images during the main and recovery phase of a CIR storm on 22 July 2009. The global spatial ion images taken at different times, along with solar wind data, geomagnetic activity indices, geosynchronous orbit observations, and in situ measurements from the THEMIS mission provide a picture of the evolution of the ring current during both the main phase and early recovery phase of the storm. Major features of the evolution are consistent with expectations based upon time dependent geomagnetic indices, e.g., SYM/H and ASY/H, and geosynchronous orbit detection of dipolarizations from GOES 11 and 12. Direct comparisons are made with in situ THEMIS ESA and SST spectral measurements. The peak energy of the ion spectrum in the ring current is seen to decrease in the recovery phase. The time evolution of the ion energy spectra over the range from 2.5 to 97.5 keV at the spatial peaks of the ring current in the inner magnetosphere obtained from ENA images is presented for the first time.

**Citation:** Perez, J. D., E. W. Grimes, J. Goldstein, D. J. McComas, P. Valek, and N. Billor (2012), Evolution of CIR storm on 22 July 2009, *J. Geophys. Res.*, *117*, A09221, doi:10.1029/2012JA017572.

## 1.  Introduction

[2]   Geomagnetic storms are an important component of space weather. The class of storms driven by corotating inter-action regions (CIRs) originating at coronal holes on the Sun [*Krieger et al.*, 1973; *Tsurutani et al.*, 2006] is especially interesting because while they are generally weaker storms, they often result in more efficient coupling into the Earth's magnetosphere [*Turner et al.*, 2006].

[3]   *Valek et al.* [2010] reported observations of energetic neutral atom (ENA) images from the TWINS mission [*McComas et al.*, 2009a] for a storm on 22 July 2009 that we will classify in this study as a CIR storm. The fact that the TWINS mission has two satellites provides nearly continuous coverage of the storm over a period of 8 h, TWINS1 during the main phase and TWINS2 during the early recovery phase, in which equatorial ion intensities can be extracted from the TWINS ENA images. The spatial ion images extracted from ENA images taken at different times coupled with solar wind data, geomagnetic activity indices, geosynchronous orbit observations, and in situ measurements from the THEMIS mission [*Angelopoulos*, 2008] provide a picture of the spatial and temporal evolution of the ring current during both the main

phase and early recovery phase of the storm. We describe how major features of the evolution appear to be consistent with expectations based upon time dependent geomagnetic indices, e.g., SYM/H and ASY/H, and geosynchronous orbit detection of dipolarizations from GOES 11 and 12. In situ THEMIS ESA [*McFadden et al.*, 2008] and SST [*Angelopoulos*, 2008] spectral measurements are compared with the temporal and spatial evolution of the energy dependence of the trapped ions in the ring current obtained from the deconvolution of TWINS ENA images.

[4]   In section 2, the data sources used in this study are described. In section 3, the data is presented and illustrated. In section 4, the implications and conclusions to be drawn from comparing the various data sets are discussed. Section 5 summarizes the results of this study. Appendix A presents in detail the methodology used to extract the ion intensities from the TWINS ENA images. Appendix B describes the method used to obtain energy spectra from the deconvolved ion intensities.

## 2.  Data Sources

[5]   In this section, we describe the satellite instruments and techniques of analysis used to produce the data for the geomagnetic storm of 22 July 2009 presented in section 3.

### 2.1.  Solar Wind and Geomagnetic Indices

[6]   The solar wind parameters as a function of time are obtained from the OMNI web site, http://omniweb.gsfc.nasa. gov/omsc_min.html. This data set compiled by NASA's Space Physics Data Facility includes data from ACE, Wind, IMP 8 and Geotail satellite missions. The data is shifted in time to the bow shock nose. Field and plasma parameters determined at an appropriate time and the bow shock model

---

[1]Physics Department, Auburn University, Auburn, Alabama, USA.
[2]Southwest Research Institute, San Antonio, Texas, USA.
[3]Department of Physics and Astronomy, University of Texas at San Antonio, San Antonio, Texas, USA.
[4]Department of Mathematics and Statistics, Auburn University, Auburn, Alabama, USA.

Corresponding author: J. D. Perez, Physics Department, Auburn University, Auburn, AL 36849, USA. (perez@physics.auburn.edu)

of *Farris* and *Russell* [1994] with the magnetopause model of *Shue et al.* [1997] are used to determine the position of the bow shock.

## 2.2. Magnetic Field at Geosynchronous Orbit

[7] The NOAA GOES satellites monitor the space weather conditions at geosynchronous orbit. For this study, we are interested in the $z$ component of the magnetic field in the Earth's tail as an indicator of dipolarizations during geomagnetic storms. We present data from GOES 11 and 12 provided by Goddard Space Flight Center Space Physics Data Facility CDAWeb, http://cdaweb.gsfc.nasa.gov/cdaweb/istp_public/. The data provider is H. Singer at NOAA SEC.

## 2.3. TWINS Instrumentation

[8] A full description of the TWINS mission of opportunity is given in *McComas et al.* [2009a]. The two spacecraft are in Molniya orbits with inclinations of 63.4°, perigee altitudes of ~1000 km, and apogees in the northern hemisphere at ~7.2 $R_E$. The spacecraft are 3-axis stabilized and provide approximately nadir pointing of the TWINS instruments. Because the two spacecrafts' orbital planes are significantly offset, the pair provide a combination of continuous magnetospheric observations from at least one TWINS satellite with several hours of simultaneous, dual platform viewing over each orbit.

### 2.3.1. TWINS ENA Instruments

[9] The TWINS imagers are based upon the "slit camera" concept [*McComas et al.*, 1998] originally flown for the MENA instrument [*Pollock et al.*, 2000] on the IMAGE satellite. This design provides the very large aperture, and hence geometric factor, required to properly image ENAs across the critical energy range from ~1 keV to several 10s of keV. For TWINS, a full image is acquired using two sensor heads that are mounted on a rotating actuator, which sweeps back and forth over an approximately Earth-centered viewing cone. Neutral atoms are detected with energies from 1 to 100 keV with $\Delta E/E \leq 1.0$ for H atoms. Full images, i.e., a full angular sweep of both heads, are taken generally every 78 s with each having a 60 s integration time. In this study, the ENA images used are integrated over 24 sweeps which corresponds to one-half hour in total time.

[10] The TWINS images are processed to have a statistically significant number of counts per pixel. Smoothing is performed on high resolution data until a desired level of minimum statistical certainty (counting statistics) is reached, uniformly across the entire image. For this study, we use counts in individual 1° × 1° pixels and sum them with their neighbors until at least 25 counts are accumulated (corresponding to 20% Poisson statistics) in order to produce smoothed number flux images. Portions of the original image that already had 25 counts are unsmoothed. Subsequently, we apply a newly developed background subtraction procedure that significantly improves the quality of the TWINS images when certain types of background are present in one of the two ENA heads. Details of both statistical smoothing as we apply it to TWINS data and the background suppression procedure are provided in *McComas et al.* [2012, Appendix A]. This technique that produces statistically smoothed images has also been applied successfully to the ENA measurements on IBEX [*McComas et al.*, 2009b].

### 2.3.2. Ion Intensity From the TWINS ENA Images

[11] A technique for extracting equatorial ion pitch angle distributions from ENA images is described in Appendix A. From each image covering a specific energy range, pitch angle distributions are obtained at all points in the equator. In this study, we show equatorial ion distributions integrated over all pitch angles. It is also assumed that the ions are hydrogen.

[12] The uncertainties, $\sigma_\alpha$ in equations (A3) and (A9) of Appendix A, in each pixel are an essential part of the process of extracting ion distributions from the ENA images. In this study, they are estimated by using ENA images are integrated over approximately 30 min, i.e., 24 sweeps or single images from the instrument. Then the second moment of the 24 individual images is used as the estimate of the $\sigma_\alpha$ values in the time-integrated image.

[13] The TWINS ENA images used in this study are integrated over energy bands equal to the central energy, e.g., an image centered at 25 keV is integrated from 12.5 to 37.5 keV. To obtain energy spectra, images centered at energies from 5 to 65 keV in 5 keV steps are used. Particularly at the higher energies, the bands overlap significantly. To extract physically meaningful energy spectra, the equatorial ion intensities integrated over pitch angle are first determined at the observed central energies as described in Appendix A. Ion intensity energy spectra are then determined using the method described in Appendix B.

## 2.4. THEMIS

[14] The THEMIS (Time History of Events and Macroscale Interactions during Substorms) mission [*Angelopoulos*, 2008] was launched on 17 February 2007 to determine the trigger and large-scale evolution of substorms. The mission employs five identical satellites. Data from the electrostatic analyzer (ESA) [*McFadden et al.*, 2008] and the solid state telescope (SST) [*Angelopoulos*, 2008] instruments are used in this study.

[15] The THEMIS ESA measures energetic particles over the energy range from a few eV up to 25 keV. The instrument consists of a pair of "top hat" electrostatic analyzers with common 180° by 6° fields-of-view that sweep out $4\pi$ steradians each 3 s spin period. Particles are detected by microchannel plate detectors. Background is subtracted from the THEMIS flux, and confidence levels are estimated to be approximately 10%. In this study, the THEMIS ESA data is mapped to the SM equator using the same magnetic field model used in obtaining the ion distributions.

[16] The THEMIS SST measures energetic ions over the energy range from 25 keV to 6 Mev. Only the interval from 25 to 100 keV will be used in this study. The angular coverage includes 4 theta look directions and 16 phi sectors. Theta and phi are in "DSL" coordinates described in *Angelopoulos* [2008]. The Z axis is along the spin axis of the satellite, Y is the cross product of the sun direction with Z and X completes the right-handed coordinate system. In this study, the THEMIS SST data are mapped to the SM equator using the same magnetic field model used in obtaining the ion distributions, and confidence levels are estimated to be approximately 10%.

[17] $O^+$ ions can be a significant contribution to the trapped ion population in the ring current during geomagnetic storms [*Kistler et al.*, 1989]. *Mitchell et al.* [2003] showed how $O^+$
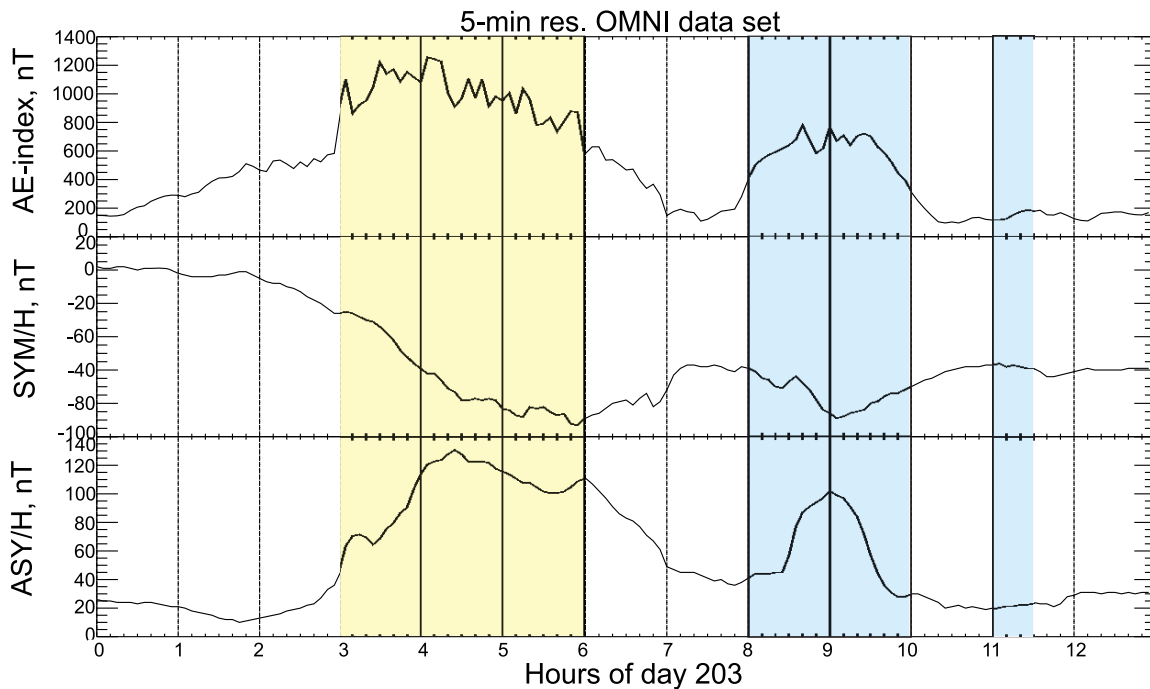
**Figure 1.** Geomagnetic activity parameters for 0000–1200 UT, 22 July 2009 from the OMNI data set at the Space Physics Data Facility of the Goddard Space Flight Center, http://omniweb.gsfc.nasa.gov/. The yellow (blue) shading shows the main (recovery) phase time period for which results are presented in this study.

could be distinguished from $H^+$ in ENA images. *Ohtani et al.* [2005] studied the variations of $O^+$ and $H^+$ during storm-time substorms using ENA images from the HENA [*Mitchell et al.*, 2000] instrument onboard the IMAGE [*Burch*, 2000] satellite. The development of a method to distinguish $O^+$ and $H^+$ in TWINS ENA images is underway. In this study, the ENA images are assumed to be protons only, so that when there are indications of a strong $O^+$ component, deconvolutions are not presented for those times.

## 3. Data

[18] In this section, we present and describe the data that depicts the spatial structure and time evolution of the geomagnetic storm on 22 July 2009 during the main phase and the first 6 h of the recovery phase.

### 3.1. Geomagnetic Activity

[19] Figure 1 shows the geomagnetic activity during the 22 July 2009 storm. The AE index shown in the first panel provides a measure of global electrojet activity in the auroral region usually associated with substorms. In the second panel, SYM/H measures the geomagnetic disturbance of the horizontal, longitudinally symmetric component of the Earth's magnetic field. In the third panel, ASY/H describes the geomagnetic disturbance of the horizontal, longitudinally asymmetric component of the Earth's magnetic field. It correlates well with the AE index and is a measure of the asymmetry in the ring current.

[20] The SYM/H shows that the main phase of the storm begins at about 0200 UT without a sudden storm commencement. The storm reaches its maximum strength when SYM/H reaches a minimum of about −90 nT just before

0600 UT. After a recovery period of about an hour, SYM/H levels off before falling to another minimum just after 0900 UT. Recovery resumes and levels off at about −40 nT by 1100 UT. There is a sharp rise in AE at 0300 UT followed by a slow decline from 0430 to 0700 UT. A second weaker peak in AE occurs between 0800 and 1000 UT. As expected the ASY/H has similar characteristics but rises after AE and descends before AE between 0900 and 1000 UT.

### 3.2. Solar Wind Parameters

[21] The solar wind parameters for the same period of time are shown in Figure 2. The first panel shows $B_y$ in the GSM frame of reference. Note that it is increasingly negative during the main phase reaching a minimum of approximately −16 nT at the same time as minimum SYM/H. It rises to a peak near 0 nT and then falls rapidly to approximately −13 nT during the broad peak in AE between 0800 and 1000 UT. It rises again to 5 nT just before 1100 UT. The second panel gives $B_z$, the north/south interplanetary magnetic induction. It is negative and decreases slowly to approximately −17 nT until it starts to increase at approximately 0430 UT becoming positive just before SYM/H reaches its minimum and the main phase ends. After reaching a peak of approximately 10 nT, It falls once more to a minimum at about 0830 UT followed by a sharp rise to positive values, near the time of a second minimum in SYM/H, from whence it oscillates about 0. The solar wind speed in the third panel increases steadily during the period shown. In the fourth panel, the solar wind density begins to increase at 0100 UT, just before the start of the storm and reaches a peak of more than 45 $cm^{-3}$ before it falls sharply prior to the peak in the storm. It then declines slowly during the recovery phase.
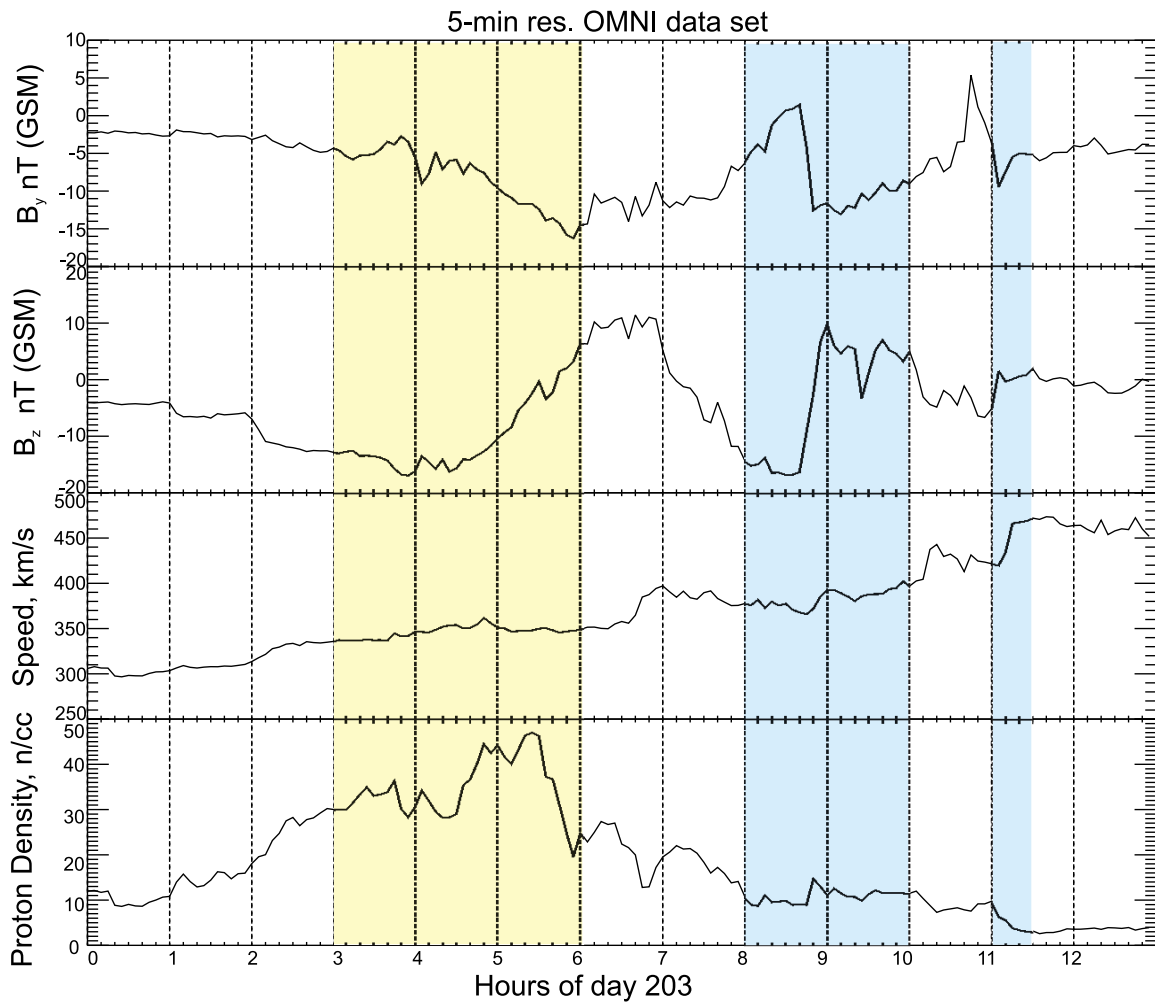
**Figure 2.** Solar wind parameters for 0000–1200 UT, 22 July 2009 from the OMNI data set at the Space Physics Data Facility of the Goddard Space Flight Center, http://omniweb.gsfc.nasa.gov/. The measurements are time shifted to the nose of the bow shock. The yellow (blue) shading shows the main (recovery) phase time period for which results are presented in this study.
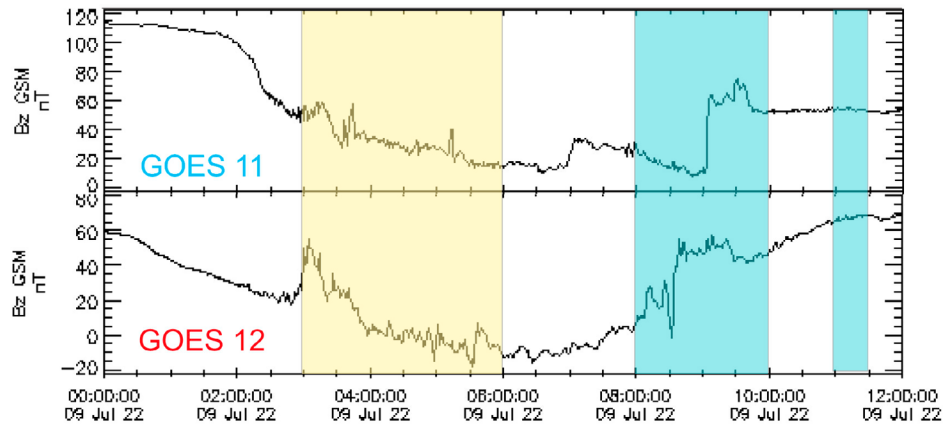
### 3.3.  Geosynchronous Orbit

[22]  The northward component of the magnetospheric magnetic induction at geosynchronous orbit during this time period is shown in Figure 3 from the GOES 11 and 12 satellites. The locations of both satellites are shown in Figure 4.

[23]  Before 0600 UT, both show a general decrease in $B_z$ indicating a general stretching of the field in the tail. For GOES 11, the decrease begins at about 0200 UT when the satellite is near dusk. There is then a weak oscillation between 0300 and 0400 UT when the satellite is at about 1900 MLT. For GOES 12, which is more toward midnight, the decrease begins at 0000 UT. A strong oscillation occurs at the same time as the weak oscillation seen by GOES 11 when GOES 12 is in the dusk/midnight sector. After 0600 UT, both show a general increase in $B_z$. But for GOES 11, there is a very sharp rise just past 0900 UT and then a leveling off just before 0100 UT, when the satellite is near midnight. For GOES 12 when it is in the pre-dawn sector, there is a sharp rise at 0830 UT about one-half hour prior to the rise observed by GOES 11.

### 3.4.  TWINS

[24]  While much can be learned directly from analysis of the ENA images, the emphasis in this study is upon the ion distributions that can be extracted from the ENA images. Thus we focus upon those periods of time in which the ENA images are suitable for deconvolution. During the main phase of the storm, TWINS 1, which was high above the north pole on the dawn side, provides the ENA images between 0300 and 0630 UT. This period is shown in yellow in Figures 1–3. During the recovery phase of the storm, TWINS 2, which was high above the north pole in the dawn/midnight sector, provides the ENA images from 0800 to 1000 UT and 1100–1130 UT. This period is shown in blue in Figures 1–3. The period between 0630 and 0800 UT, when TWINS 1 is turning off and TWINS 2 is rising, has strong backgrounds because of the relatively low L values at the time. We also find that the method we use to estimate uncertainties gives values that are too large making it impossible to obtain good deconvolutions. During the period 1000–1100 UT, there are indications that there are significant $O^+$ ions, consistent with

**Figure 3.** The *z* component of the GSM magnetic induction at geosynchronous orbit as observed by GOES 11 and 12 from 0000 to 1200 UT, 22 July 2009 from the NOAA Space Weather Prediction Center, http://www.swpc.noaa.gov/Data/goes.html. The yellow (blue) shading shows the main (recovery) phase time period for which results are presented in this study.

the AE activity at this time, in the ENA images. The deconvolution of these images will be the focus of a future study.

### 3.4.1. Main Phase

[25] The columns of Figures 5a and 5b show a typical set of ENA images and the resulting ion distributions at 0345 UT on 22 July 2009 for energy bands centered at 5, 10, 15, 20, 30, 40, 60 keV. The full width of each band is equal to the central energy. The first column shows the ENA images plotted in a perspective in which the pixels are shown where their lines-of-sight intersect the SM equator. Each pixel is a $4° \times 4°$ projection. There are 15 circles of 90 pixels. The outermost radius is therefore at $60°$ corresponding to a distance that is dependent on the height of the satellite. The center of the circles is along the central line-of-sight of the ENA instrument. The third column shows the equatorial ion intensity averaged over pitch angle, i.e., the differential directional number flux, as determined using the method described in Appendix A. The second column shows the ENA images obtained from the deconvolved ion distributions, i.e., the fit to the data. Each energy, i.e., each row, uses a different color bar in order to emphasize the spatial variations. The color bars for each energy band are the same in the first and second columns so a direct comparison is appropriate. The low altitude emissions (LAEs) discussed in Appendix A are the brightest pixels in the ENA images. The fits, i.e., the comparison between the first and second columns are not perfect; they are not expected to be, as a $\chi^2 = 0$ would indicate an attempt to extract more information from the images than was statistically significant. Each, however, has a $\chi^2 = 1$. The projection format for the first column (TWINS Images) and the second column (Calculated ENAs) was chosen to emphasize the comparison between the two images. Geophysical interpretations are made from the ion distributions (Equatorial Ions).

[26] There are several features of the energy dependent ion spatial distributions of the deconvolved equatorial ion flux (third column of Figures 5a and 5b) to be noted. The highest ion intensity is in the 30 keV distribution. As we shall see below, this does not necessarily mean that the peak energy in the ion intensity is at 30 keV. Furthermore, between 5.0 and 30.0 keV, there are two peaks in the spatial distributions, one

at 4.5 $R_E$, 23 MLT, and a second peak (weaker for most energies) at 6.5 $R_E$, 19 MLT. The strength of the second peak grows with energy. Above 50 keV, there are also two peaks, one at 4.5 $R_E$ and 21 MLT, the second at 6.0 $R_E$ and 1 MLT. Aside from small differences in MLT, the main features of the spatial distribution are not energy dependent, and we will use the 15.0 keV results to illustrate temporal behavior.

[27] Figure 6 shows the energy spectra at the locations of the peaks described in the previous paragraph. The blue data points are the values of the ion intensities in the spatial distributions shown in the third column of Figures 5a and 5b. The blue horizontal bars illustrate the overlap of the energy bands in the data (also see Appendix B). The vertical error bars are those resulting from the statistical nature of the
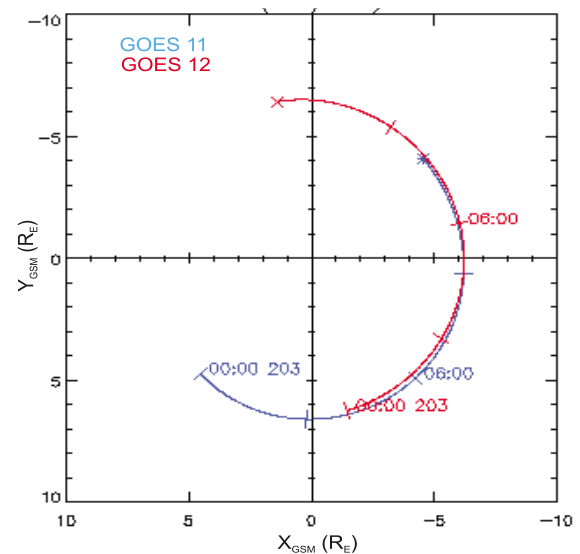


**Figure 4.** The position in the $X_{GSM}$ - $Y_{GSM}$ plane of GOES 11 and 12 from 0000 to 1200 UT, 22 July 2009 from the NOAA Space Weather Prediction Center, http://www.swpc.noaa.gov/Data/goes.html.
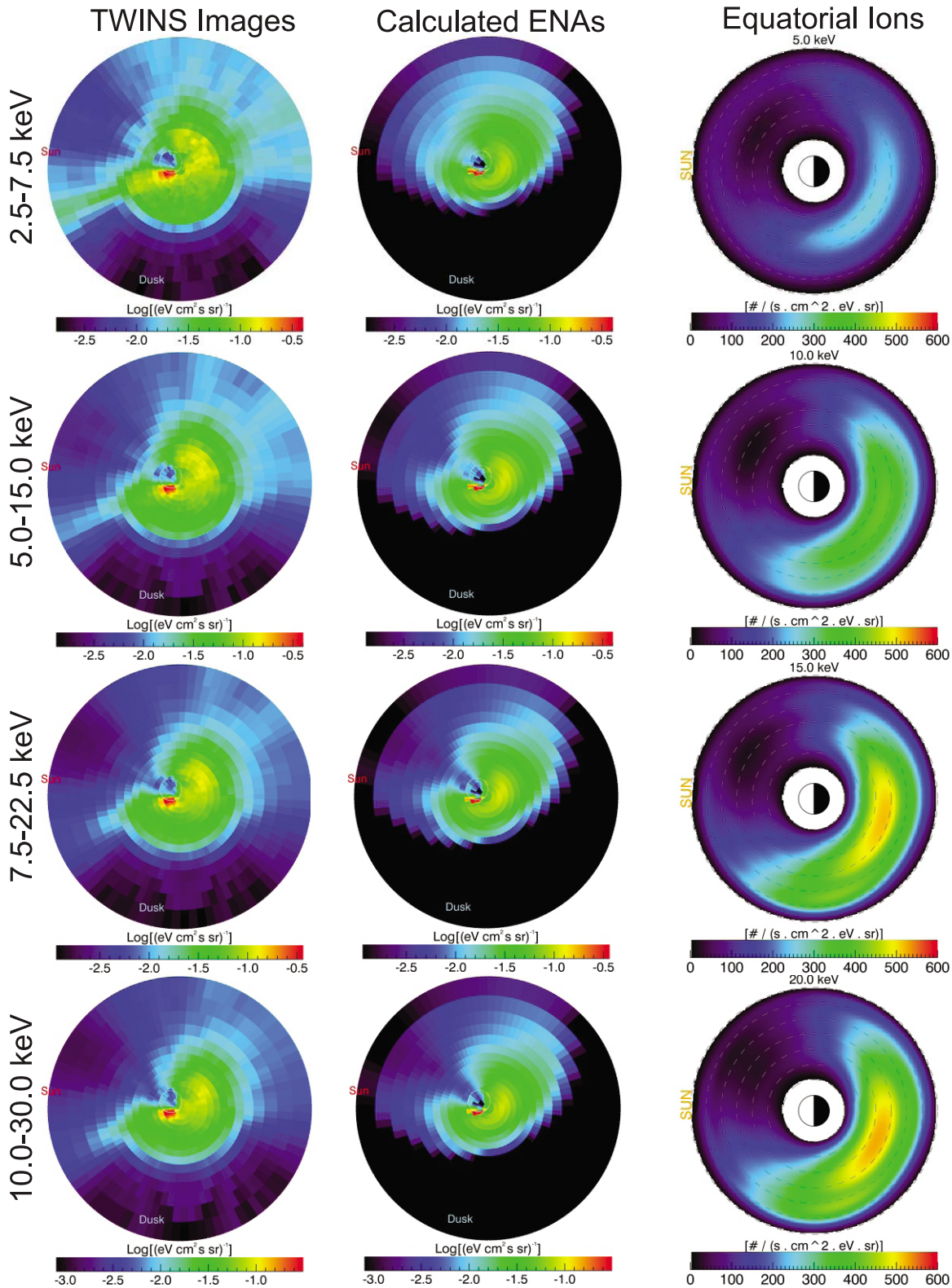
**Figure 5a.** ENA images from TWINS1 and the deconvolved equatorial ion intensity averaged over pitch angle at 0344 UT, 22 July 2009, for energy bands centered at 5.0, 10.0, 15.0, and 20.0 keV. The first column is the logarithm to the base 10 of the ENA intensity measured by TWINS1. The second column is the same quantity obtained from the deconvolved intensity in the third column. The first and second columns have the same color bars for each energy. The ion intensity in the third column is plotted on the same linear color bar for all energies. The position of TWINS1 is $\{-1.0, -2.7, 6.4\}$ RE in the SM coordinate system.
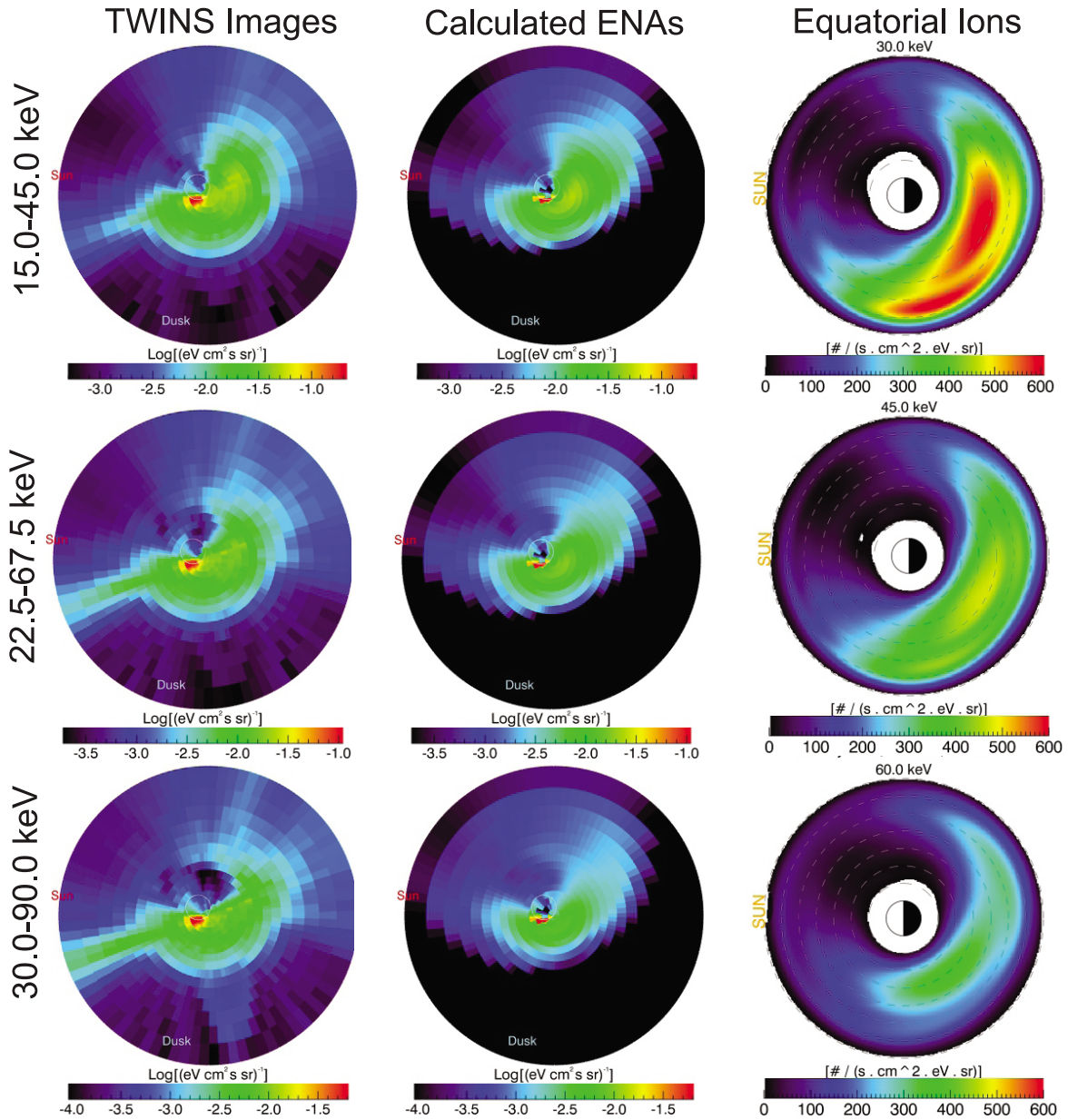
**Figure 5b.** Same as Figure 5a but for 30.0, 45.0, and 60.0 keV.

process used to extract the ion distributions from the ENA images as explained in Appendix A. It is important to note that there are several unquantified contributions to the total uncertainties in the results of the deconvolution, e.g., the magnetic field model, the model for the density of the geocorona, violations of the first adiabatic invariant, and possible mixture of oxygen ENAs with the hydrogen that cannot be included in the statistical confidence levels shown. These elements of the deconvolution generate uncertainty in the spatial dimension as well as in the magnitude of the ion intensity. The red lines are point energy spectra obtained from the blue data and represent the intensity energy spectrum obtained from the TWINS ENA images. The dashed green curve is a Maxwellian chosen to match the peak of the physical spectra shown by the red line. Since the wide energy bands at higher energies contain contributions from lower energy where the ion intensity is expected to be higher, it is not surprising that the blue values show a higher energy tail than the red line. What is surprising is that the energy spectra derived from the ENA images early in the main phase of this storm have shapes that are narrower than a comparable Maxwellian.

[28] Figure 7 shows the 15 keV spatial distributions as a function of time at one-half hour intervals during the main phase. Again the color bars are different for each time to emphasize the spatial distributions. The maximum intensity increases as a function of time until 0514 UT and then drops slightly. As a function of time the peak expands duskward and outward from 4.5 $R_E$ to 6.0 $R_E$ until moving back to 4.5 $R_E$ at 0514 UT. The ring current remains asymmetric during the main phase.
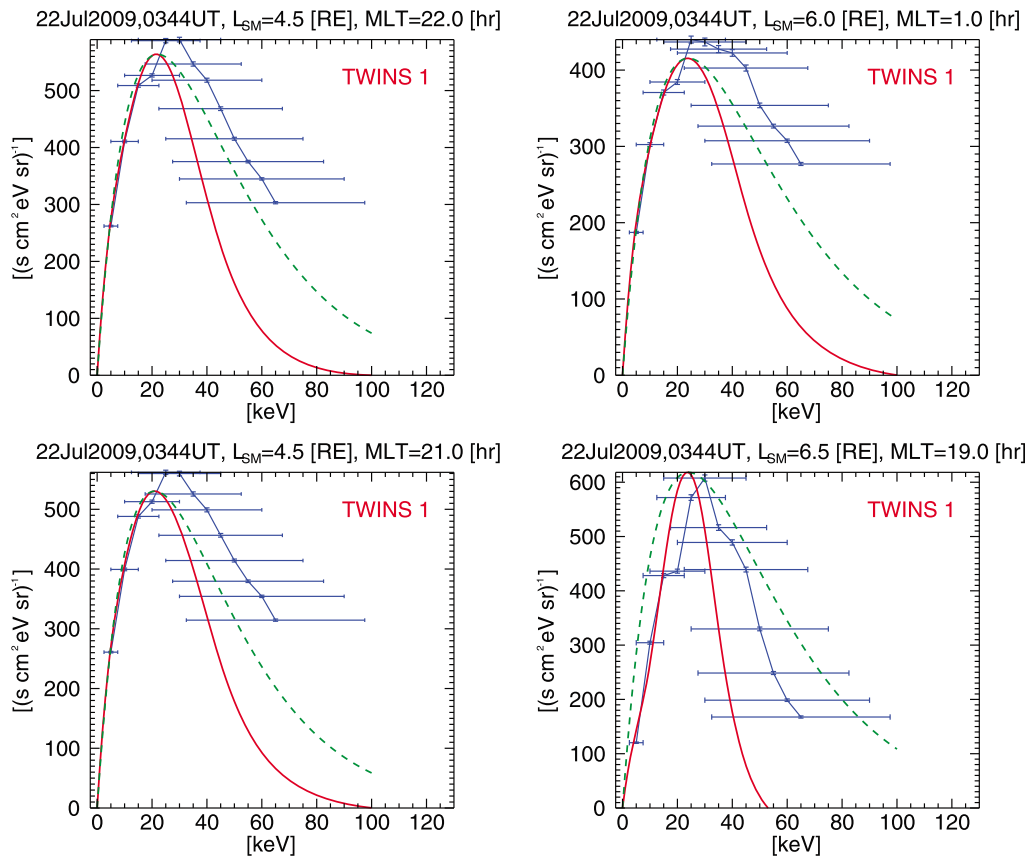
**Figure 6.** The ion energy spectrum for 4 different positions at 0344 UT, 22 July 2009. The blue points are the ion intensities obtained directly from the deconvolution, i.e., from the third column of Figures 5a and 5b, but in energy bands centered at 5–65 keV in 5 keV steps. The horizontal bars are the width of the energy bands; the vertical bars are the statistical errors from the deconvolution process. The red line is the actual energy spectrum obtained from the blue points as described in the text. The dashed green line is a Maxwellian whose temperature and amplitude were chosen to match the peak of the actual energy spectrum from the ENA images.

[29] Figure 8 shows energy spectra at the spatial peaks as a function of time in 1 h intervals. The peak in the energy spectra decreases with time indicative of a falling temperature. By 0544 UT (bottom plot), the energy spectrum is moving toward Maxwellian. The magnitude of the peak intensity shows an increase consistent with the decrease in SYM/H.

### 3.4.2. Recovery Phase

[30] Figures 9a and 9b show the data and deconvolved ions as a function of energy at 0944 UT in the same format as Figures 5a and 5b. Note that the ENA images in the first column are no longer dominated by the LAEs. The direct ENA data (first column) and the image (second column) obtained from the deconvolved intensity (third column) show excellent agreement. Again the location of the peak in the spatial distribution is relatively energy-independent. Also note the increased symmetry of the ring current at the higher energies.

[31] Figure 10 shows the 15 keV equatorial ion intensities integrated over pitch angle at a series of times. Prior to 0900 UT, the peak in the ring current is in the dawn sector, while after 0900 UT, the peak has moved to the post-midnight sector until the ring current becomes symmetric at 1114 UT. At 0914 UT, there is the remnant of the dusk peak from earlier together with the new, dominant peak between
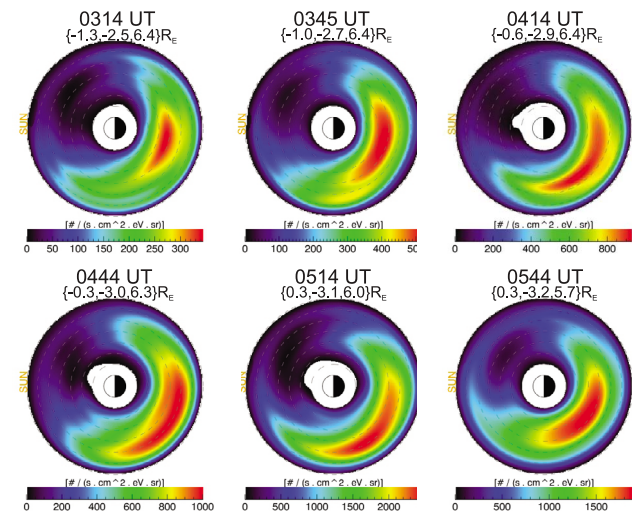


**Figure 7.** The time evolution of the equatorial ion intensity averaged over pitch angle for the energy band centered at 15 keV from 0300 to 0600 UT, 22 July 2009. The color bars are different for each time to emphasize the spatial distributions. The position of TWINS 1 is given in the SM coordinate system in the format {x,y,z}.
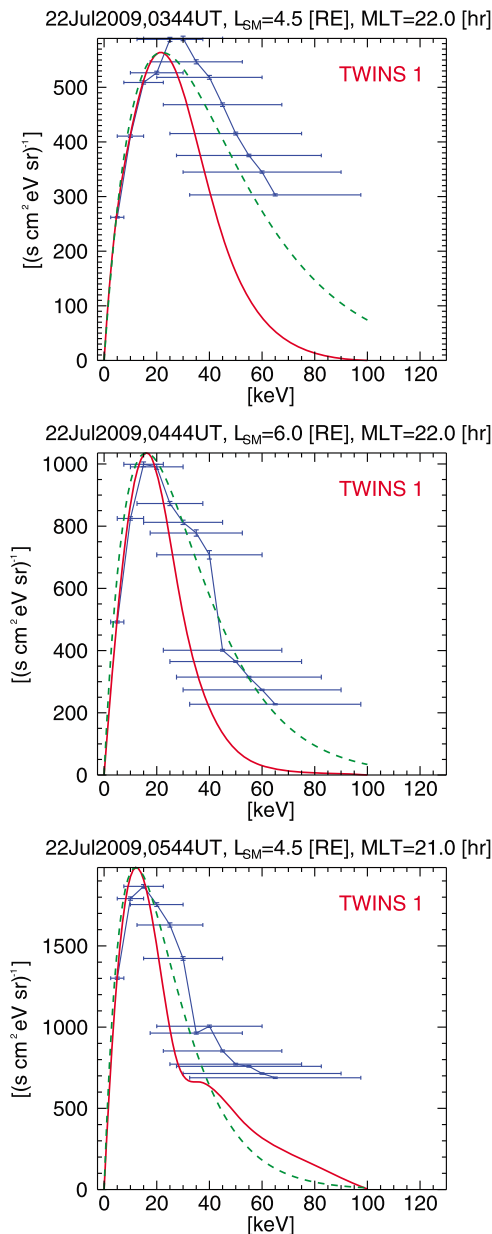
**Figure 8.** The time evolution of the energy spectrum of the equatorial ion intensity averaged over pitch angle from 0300 to 0600 UT, 22 July 2009. The format is the same as in Figure 6.

midnight and dawn. At 0814 UT, there are indications of a double peak in the dusk/midnight sector, one at 5.5 $R_E$ and another at 6.5 $R_E$.

[32] Figure 11 shows the energy spectra at the peaks in the distributions as a function of time from 0800 to 1000 UT in half hour intervals. (Recall that the spectrum in upper left corner labeled 0814 UT comes from an image integrated over time from approximately 0800–0830 UT. By 0944 UT the spectrum at the peak of the equatorial ion distribution has changed from having a high energy tail to nearly Maxwellian.

### 3.5. THEMIS/TWINS Comparison

[33] Two THEMIS probes "d" and "e" passed through the magnetotail during the recovery phase along essentially

identical paths separated by about 1 h. Figures 12a and 12b show the paths of the satellites plotted on top of the 15 keV equatorial ion intensities at 0914 and 0944 UT, respectively. Figures 12c–12f showing intensity vs energy spectra omit the blue points that come directly from the deconvolved equatorial distributions to focus upon comparison between the TWINS (red) and THEMIS ESA (brown and "v" symbol) and SST (blue and inverted "v" symbol) measurements. The dashed curves are Maxwellians chosen to fit the peaks of the TWINS and THEMIS spectra.

[34] The results in Figure 12 are similar in character to those found in a comparison of ion intensities deduced from ENA images produced by IMAGE/HENA and in situ measurements from CLUSTER-CIS [*Vallat et al.*, 2004]. As pointed out by *Vallat et al.* [2004], there are a number of things to be noted in interpreting such comparison. The intensities obtained from the ENA images are affected by uncertainties in the magnetic field model and the hydrogen geocorona model used. In this case, the ENA images are integrated over a half hour time period and certainly do not have the spatial resolution of the in situ THEMIS measurements. Perhaps even more important is the fact that the THEMIS measurements show extensive dynamic variations during this time period. This is illustrated in Figure 13 where combined THEMIS d ESA and SST spectra at the three times closest to the times of the comparison in Figures 12c and 12e are plotted. In Figure 13a, THEMIS d around 0914 UT shows considerable variation in the peak of the spectrum which is one measure of temperature and changes in the tail between 15 and 30 keV. In Figure 13b, THEMIS d around 0944 UT shows considerable variation in the magnitude and energy of the peak as well as changes in the 15–40 keV region. The features to be noted in Figure 12 are (1) the non-Maxwellian high energy tail at 0914 UT in both the TWINS and THEMIS results (Figure 12c) whereas (2) later and at smaller radius, both instruments show Maxwellian-like distributions and tails (Figure 12e), (3) the different low energy peaks in the THEMIS e and TWINS results at 0914 UT but non-Maxwellian tails in both (Figure 12d), and (4) the Maxwellian-like distribution from TWINS and the high energy non-Maxwellian tail from THEMIS e at 0944 UT (Figure 12f).

## 4. Discussion

[35] Despite the relatively slow change in the solar wind, it is the non-steady north/south component of the interplanetary magnetic field (see Figure 2) that leads us to classify the storm on July 22, 2009 as a CIR driven storm. CIRs, co-rotating interaction regions, are large scale structures in the heliosphere that generally produce weak storms defined as those with minimum SYM/H > −100 nT (see Figure 1). The relatively slow rise of the solar wind density and then rapid fall near the peak of the storm is another characteristic of a CIR storm. A review of CIR storms is given in *Tsurutani et al.* [2006].

[36] The peak in the ring current in the pre-midnight sector (see Figures 5a and 5b) is consistent with the dipolarization event seen by GOES 11 and 12 in that sector (see Figures 3 and 4) just past 0300 UT. At higher energies (see Figures 5a and 5b) the ring current peak has moved duskward consistent with expectations of energy-dependent drift in a spatially
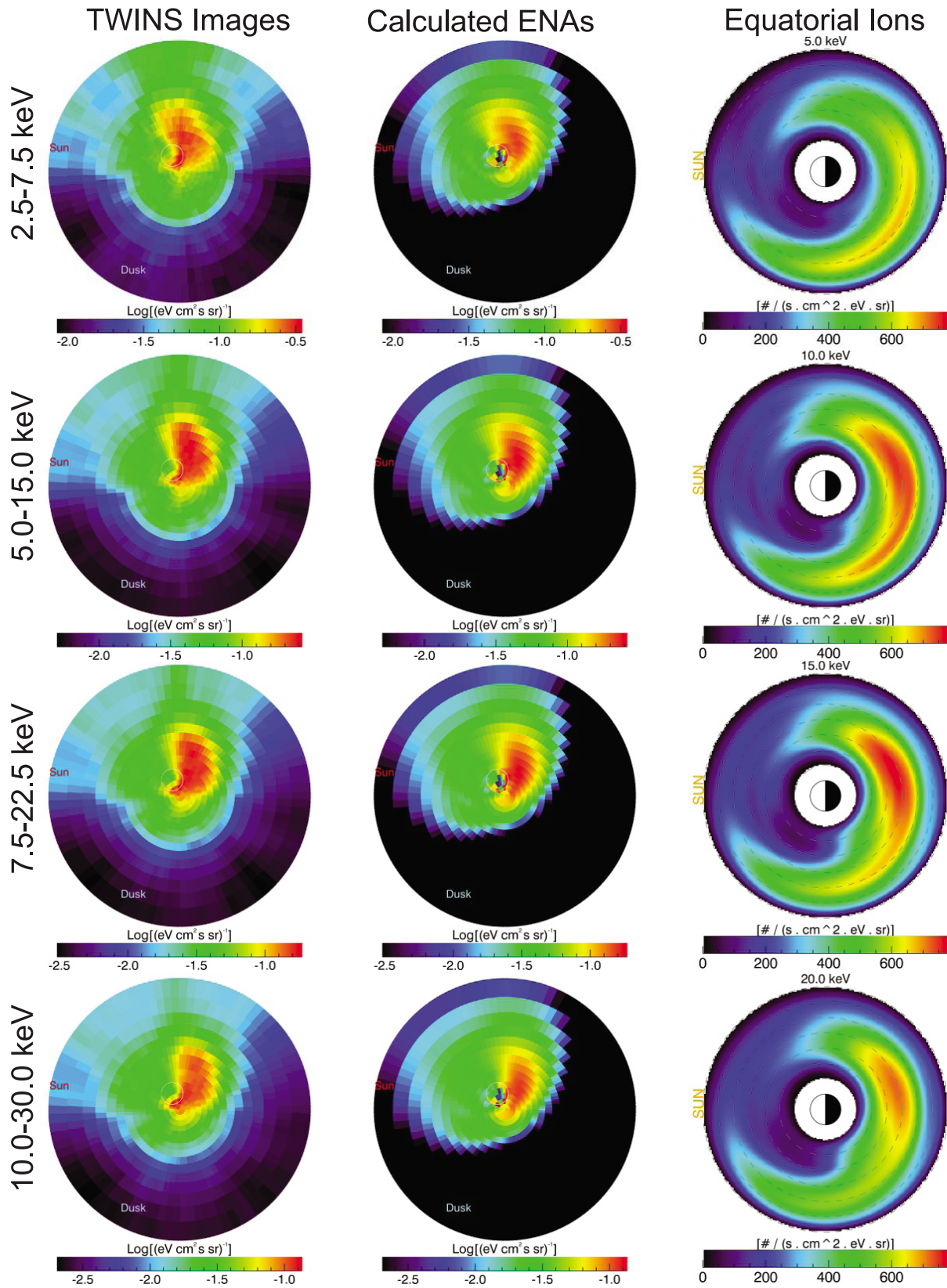
**Figure 9a.** ENA images from TWINS2 and the deconvolved equatorial ion intensity averaged over pitch angle at 0944 UT, 22 July 2009, for energy bands centered at 5.0, 10.0, 15.0, and 20.0 keV. The format is the same as Figures 5a and 5b. The position of TWINS2 is {1.8, −1.8, 6.7}RE in the SM coordinate system.
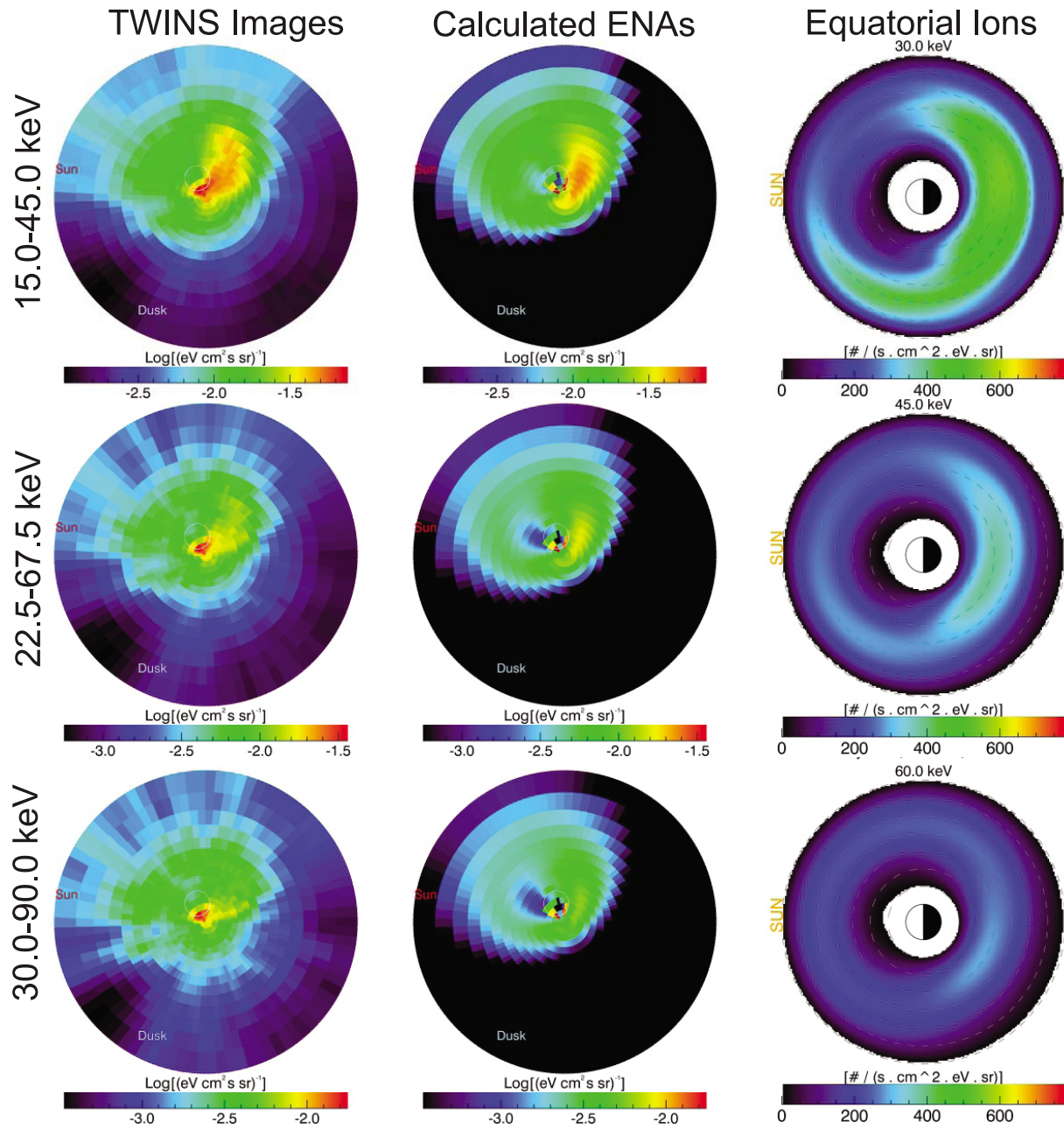
**Figure 9b.** Same as Figure 9a but for 30.0, 45.0, and 60.0 keV.

varying magnetic field. The secondary peak seen in Figures 5a and 5b at larger radial distance may be the result of the dipolarization at approximately 0330 UT as seen by GOES 11 and 12. The fact that it appears near dusk at low energies, spans the dusk-to-midnight sector at intermediate energies, and is most visible at midnight at high energies is not understood at this time. Nevertheless, the bulk of the distribution is very similar at various peak locations as shown in Figure 6.

[37] It is clear in Figures 5a and 5b that the ring current is asymmetric. This is consistent with the rising value of ASY/H shown in Figure 1 at this time. The time-dependent 15 keV equatorial intensities in Figure 7 show that the ring current remains asymmetric during the main phase of the storm as expected from the ASY/H observations.

[38] During the period 0300–0600 UT of the main phase, SYM/H decreases from $-25$ to $-90$ nT, while the maximum in the peak ion distribution shown in Figure 8 increases from 570 (eV cm$^2$ s sr)$^{-1}$ at 0344 UT to a maximum of 1800 (eV cm$^2$ s sr)$^{-1}$ at 0544 UT. It is the energy in the ring current, however, that is expected to be correlated with SYM/H, which is the integral under the red curve in Figure 8. The shift in the peak to lower energy and a narrowing of the peak as well as the changing area of the ring current as shown in Figure 7 must be analyzed for a detailed quantitative comparison with SYM/H. Such an analysis of ring current energy will be the focus of a future study.

[39] During the recovery phase, the ENA images are no longer dominated by the LAEs (see Figures 9a and 9b) as originally reported by *Valek et al.* [2010]. We also see that
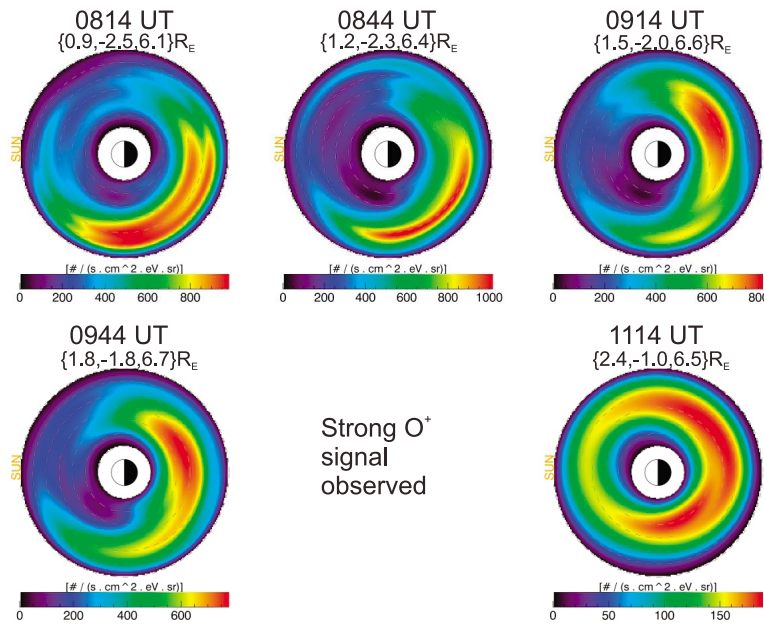
**Figure 10.** The time evolution of the equatorial ion intensity averaged over pitch angle for the energy band centered at 15 keV from 0800 to 1130 UT, 22 July 2009. The color bars are different for each time to emphasize the spatial distributions. The position of TWINS 2 is given in the SM coordinate system in the format {x,y,z}.
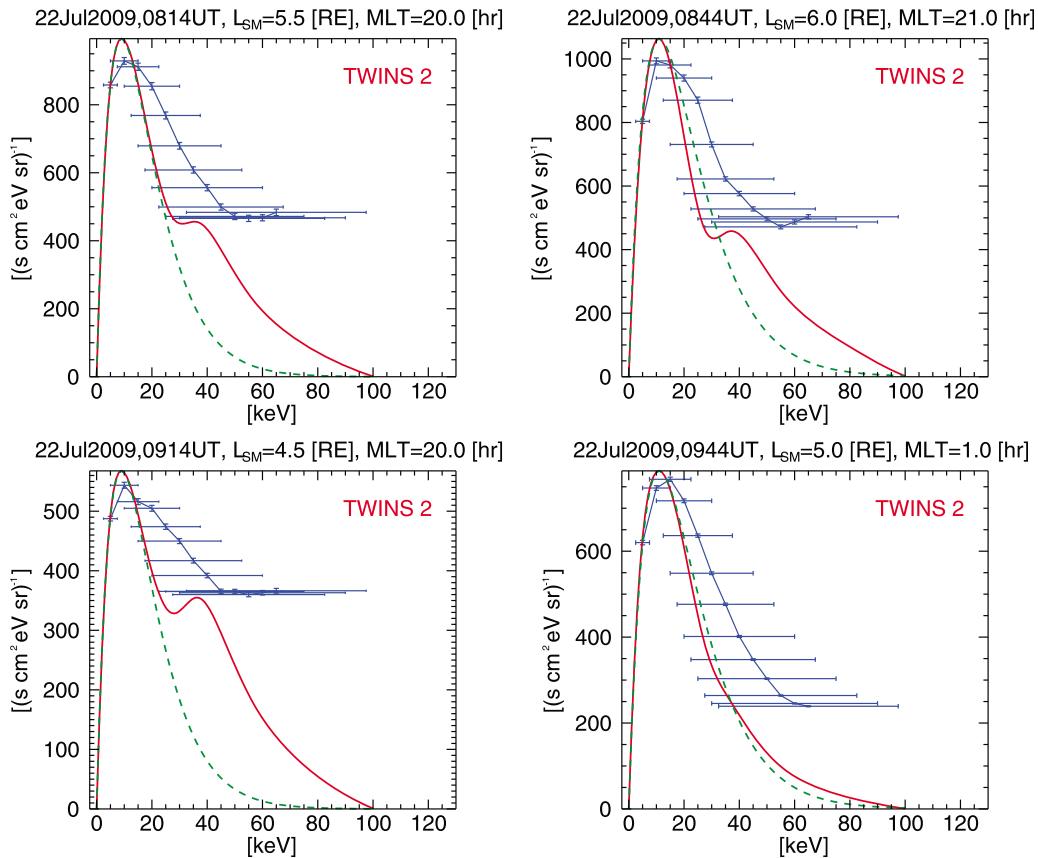


**Figure 11.** The time evolution of the energy spectrum of the equatorial ion intensity averaged over pitch angle from 0800 to 1000 UT, 22 July 2009 near the peaks of the spatial distributions. The format is the same as in Figure 6.
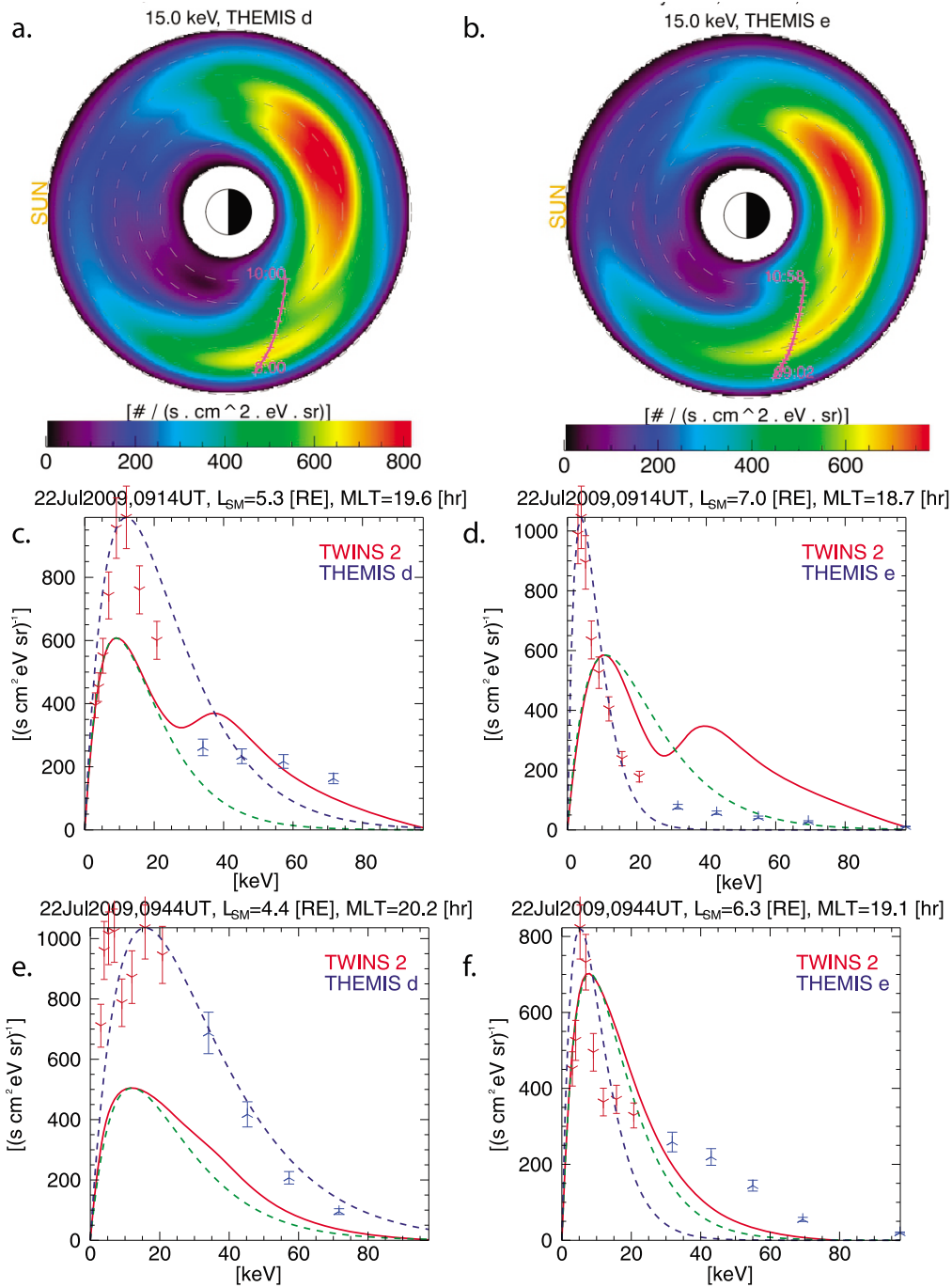
**Figure 12.** Comparison of energy spectrum obtained from TWINS ENA global images and THEMIS probes d and e local measurements. The path of THEMIS d and e from (a) 0800 to 1000 UT and (b) 0900 to 1100. (c–f) Energy points from the ESA instrument (brown "v") from 2.5 to 25 keV and the SST instrument (blue inverted "v") from 30 to 100 keV. The energy spectra from the TWINS data (red) is obtained as described in Appendix B. The dashed curves are Maxwellians for THEMIS (dark blue) and TWINS (green).

the ring current is more symmetric at higher energies, consistent with the expectations of energy-dependent drift in a spatially varying magnetic field. The time-dependent 15 keV peaks (see Figure 10) show that the ring current becomes weak and symmetric by 1114 UT, but does not clearly follow the ring current asymmetry consistent with the peak in ASY/H at 0900 UT in Figure 1. More detailed analysis of

the ring current plasma pressure is needed and will be a focus of future study.

[40] The shift of the ring current peak from the premidnight sector where it was in the main phase to the post-midnight sector at 0914 UT (see Figure 10) matches well with the dipolarization event seen between 0830 and 0900 UT by GOES 11 and 12 (see Figure 3). Note that
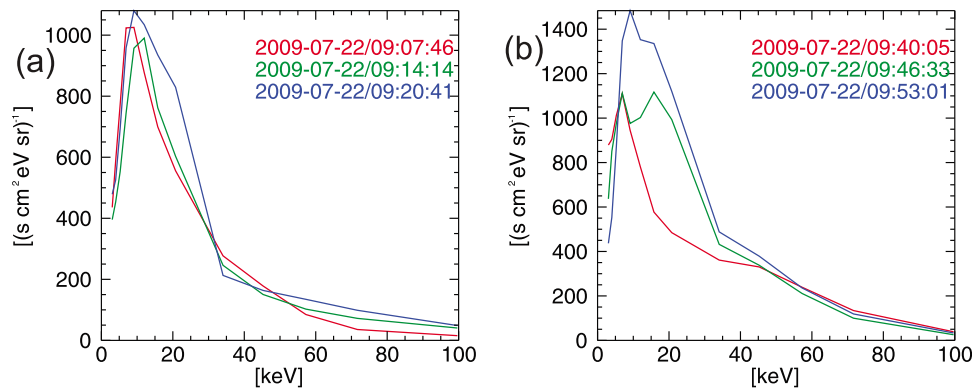
**Figure 13.** Combined THEMIS d ESA and SST spectra centered around times corresponding to Figures 12c and 12e.

GOES 12 at approximately 0400 MLT sees this dipolarization about 30 min before GOES 11 near midnight strongly supporting the occurrence of the peak in the ring current in the post-midnight sector.

[41] The highest peak of the ion intensity shown in Figure 11 occurs near 0844 UT just prior to the secondary minimum in SYM/H just past 0900 UT (see Figure 1). As explained above, it is the ring current energy which is the appropriate integral over energy and space of the ion intensities, and this will be the focus of a future study.

[42] Comparison of ion intensity energy spectra at the peaks of the ring current in both the main phase and the recovery phase of the same storm have been presented in this study. The peak in the energy spectra which is an indicator of temperature is higher, above 20 keV, in the middle of the main phase and shifts to between 10 and 15 keV at the end of the main phase (see Figure 8). In the recovery phase, the peak is generally near or below 10 keV (see Figure 11), showing a general decrease in ring current temperature during the storm. The shape of the spectra at the peaks of the trapped ion distribution also evolves. Early in the main phase, the ion energy spectrum is narrower than a corresponding Maxwellian but moves to near Maxwellian just prior to the minimum SYM/H (see Figure 8). In the recovery phase in the time period that includes a peak in AE and ASYM/H, the TWINS ion spectrum shows a non-Maxwellian high energy tail that becomes Maxwellian.

[43] Direct comparison of the ion intensity spectra obtained from TWINS ENA images with THEMIS in situ measurements during the recovery phase confirm the dynamic nature of the spectra during this time period. The fact that there is not detailed agreement over the entire spectrum, however, is not at all surprising. The temporal and spatial resolutions of the two measurements are very different. It is also true that THEMIS is an energy measurement and TWINS is a velocity measurement, thus the energy spectra are affected very differently by any mix of $O^+$ and $H^+$ in the ring current.

## 5. Summary

[44] The spatial and temporal evolution of ion intensities have been extracted from TWINS ENA images during the main and recovery phase of a CIR storm on 22 July 2009. Combining geomagnetic activity indices, solar wind data, geosynchronous orbit observations and THEMIS in situ measurements with the deconvolved ion intensities provides a picture of the storm kinetics of a single CIR storm over an extended period of time.

[45] The strength and location of peaks in the trapped ions in the ring current are compared with the SYM/H and ASY/H indices and dipolarizations observed by GOES 11 and 12 at geosynchronous orbit. The temporal changes of the shapes of ion intensity spectra at the peaks in the ring current during the main and recovery phase of the same storm have been determined. Early in the main phase, the peak is in the pre-midnight sector with the highest intensity above 20 keV. The peak energy moves down by the end of the main phase to between 10 and 15 keV. Early in the main phase spectra are narrower than the corresponding Maxwellian but become Maxwellian-like at the end of the main phase. During the recovery phase, the energy peak moves to near or below 10 keV and a high energy tail is evident, but the spectrum becomes Maxwellian later after a peak in AE and ASYM/H. The position of the intensity peak moves to the post-midnight sector. The features of the intensity dependence on energy are also observed by THEMIS. Direct comparison between ion intensities from TWINS and THEMIS reveal examples of agreement and disagreement.

[46] The results of this study of an extended period of a CIR storm including both the main phase and recovery phase show a number of features that reflect on the drift physics and decay processes in the ring current. The comparison of results from global images and in situ measurements also show different views of the dynamics of the ring current. These results provide the basis for detailed analysis of the plasma pressure and energy content in the ring current that can be compared with numerical models of ring current evolution and demonstrate the ability to combine global images and in situ measurements to better understand and monitor the Earth's ring current.

## Appendix A: Description of Deconvolution Technique

### A1. Mathematics

[47] ENA images consist of a two-dimensional array of observed values. Each element of the array is a pixel in the

image. For the TWINS ENA images used in this paper, the value in each pixel is the intensity of ENAs at the instrument, i.e., the number of ENAs per unit time, energy, area, and steradians. For ENAs generated in the Earth's magnetosphere, there are two sources that must be considered. First are the ENAs created by charge exchange of plasma ions with the extended relatively rarefied hydrogen geocorona surrounding the Earth above the ionosphere. Second are those created by charge exchange of plasma ions with neutrals in the dense ionosphere, the so-called low-altitude emissions (LAE). These will be discussed in detail in section A2. The following mathematics is presented for the former, i.e., the ENAs originating from the geocorona that can be treated as optically thin. The simple model described in section A2 allows the LAEs to be treated in the same formalism.

[48] For optically thin emissions, the value in each element (pixel) in the image array can be expressed as a line-of-sight integration of the ENA intensity in the field-of-view of the pixel defined as the solid angle viewed by the designated pixel, i.e., the volume from which the ENAs can enter that pixel of the instrument, i.e.,

$$d_\alpha = \int d^3x I(\vec{x}, \vec{v}, t)\sigma_{ex}(E)n_{neutral}(\vec{x})R_\alpha(\vec{x}) \qquad (A1)$$

where

$d_\alpha$ is the measured value, i.e., ENA intensity at the instrument, for the $\alpha^{th}$ pixel,

$I(\vec{x}, \vec{v}, t)$ is the unknown source ion intensity,

$\sigma_{ex}(E)$ is the charge exchange cross section,

$n_{neutral}(\vec{x})$ is the number density of geocoronal neutrals, and

$R_\alpha(\vec{x})$ is the response function for the $\alpha^{th}$ pixel. It includes the factors that incorporate the effects of distance between the source and the instrument.

[49] In order to find the unknown ion intensity, a set of integral equations, equation (A1), must be solved.

[50] It is to be noted that for a specific energy and time, the ion intensity is still a function of three space variables giving the spatial location of the source and two angles denoting the direction of the velocity of the ENA. This means that the integral over the line-of-sight volume only contains information about one velocity value in the ion intensity at each spatial point. There is simply not enough information in a single ENA image for extracting an unknown five-dimensional, i.e., 3 space and 2 velocity direction variables, ion intensity to be a meaningful process. In other words, if the data only contains information about one velocity direction at each point in space, there is insufficient information to determine the 5D intensity at that point as a function of velocity. To make the extraction of information about the spatial and velocity dependence of the ion intensity a tractable problem, the ions are taken to be gyrotropic and assumed to move along magnetic field lines conserving their magnetic moments and energies. Then, each point in three-dimensional space can be mapped to the equator along magnetic field lines using a magnetic field model reducing the spatial variables to two. Likewise the pitch angle, the sole remaining velocity angle variable, determined by the requirement for the ion to enter the specific pixel can be mapped to the equator. Thus at each point in the equator, there is

information regarding a span of pitch angles making extraction of an equatorial pitch angle distribution possible.

[51] The method of solving the set of integral equations that has been found successful in working with this type of data [*Grimes et al.*, 2010] is to expand the unknown intensity in terms of a linear set of basis functions. A set of tricubic B-splines [*deBoor*, 1978] is used, i.e.,

$$I(r, \varphi, \cos\psi) = \sum_i \sum_j \sum_k a_{i,j,k} S_i(r)P_j(\varphi)S_k(\cos\psi) \qquad (A2)$$

where

$S_i(r)'s$ and $S_k(\cos\psi)'s$ are ordinary cubic B-splines for the equatorial radius and the cosine of the pitch angle respectively,

$P_j(\varphi)'s$ are periodic cubic splines for the equatorial angle, and

$a_{i,j,k}'s$ are the unknown expansion coefficients.

[52] The number of basis functions to be included in the summations is determined by increasing the number until the result does not change. For the work reported in this paper, 16 radial splines (with the restriction that the solution be zero at the minimum, 2 $R_E$, and maximum, 8 $R_E$, resulting in 14 radial splines), 12 periodic angular splines, and 4 pitch angle splines are included for a total of 672 basis functions. The boundary conditions on the radial part of the solution, that it be zero at the minimum and maximum radii, are necessary to restrain the solution in regions where the ENA data does not. When it appears that this may affect the result, the maximum radius can be moved outward.

[53] To enforce the requirement that the solution fit the data, the function,

$$\chi^2 \equiv \frac{1}{N_{pixels}} \sum_\alpha^{N_{pixels}} \left(\frac{d_\alpha - c_\alpha}{\sigma_\alpha}\right)^2 \qquad (A3)$$

may be minimized where the $\sigma_\alpha's$ are the uncertainties in each pixel (how these are determined for the TWINS data treated in this paper is described in section 2.3.2), and

$$c_\alpha \equiv \sum_{\{i,j,k\}} D_{\alpha,\{i,j,k\}} a_{i,j,k} \qquad (A4)$$

are the calculated ENA intensities in each pixel with the design matrix

$$D_{\alpha,\{i,j,k\}} \equiv \int d^3x\, \sigma_{ex} n_{neutral}(\vec{x})S_i(r)P_j(\varphi)S_k(\cos\psi)R_\alpha(\vec{x}) \qquad (A5)$$

representing the value in each pixel for each basis function. It is well known, however [*Press et al.*, 1992], that such an approach leads to a set of linear equations that may be numerically unstable. Some sort of regularization function must be added to the function to be minimized in order to produce reliable, numerical results. The choice of regularization function is described in the next paragraph.

[54] It is also to be noted that by its very nature the solution for the ion intensity is not unique. The simple fact that

the unknown ion intensity appears under an integral sign means that there could be more than one solution. The number and form of the solutions is certainly restricted when there is more and better quality data, for example when there is data from two different perspectives as provided by the two TWINS imagers. *Wahba* [1990] addressed this problem using the formalism of reproducing kernel Hilbert spaces and the principles of Bayesian statistics with the assumption of no prior knowledge to derive a methodology that selects the solution that meets a rigorously derived smoothness criterion. In other words, the final solution is as smooth as the data allows where smoothness is defined as minimizing a penalty function, which for the spline expansion functions used here has been shown to be [*Perez et al.*, 2001]

$$
P_{\{i,j,k\},\{l,m,n\}} \equiv \int dr \int d\varphi \int d(\cos\psi) f_{\{i,j,k\}}
$$

$$
\cdot \left(
\begin{array}{c}
\dfrac{\partial^6}{\partial r^2 \partial \varphi^2 \partial (\cos\psi)^2} + \dfrac{\partial^2}{\partial r^2} + \dfrac{\partial^2}{\partial \varphi^2} + \\[2mm]
\dfrac{\partial^2}{\partial (\cos\psi)^2} + \dfrac{\partial^5}{\partial r \partial \varphi^2 \partial (\cos\psi)^2} + \\[2mm]
\dfrac{\partial^5}{\partial r^2 \partial \varphi \partial (\cos\psi)^2} + \dfrac{\partial^5}{\partial r^2 \partial \varphi^2 \partial \cos\psi} + \\[2mm]
\dfrac{\partial^4}{\partial r^2 \partial \varphi^2} + \dfrac{\partial^4}{\partial r^2 \partial (\cos\psi)^2} + \dfrac{\partial^4}{\partial \varphi^2 \partial (\cos\psi)^2} + \\[2mm]
\dfrac{\partial^4}{\partial r \partial \varphi \partial (\cos\psi)^2} + \dfrac{\partial^4}{\partial r \partial \varphi^2 \partial \cos\psi} + \\[2mm]
\dfrac{\partial^4}{\partial r^2 \partial \varphi \partial \cos\psi} + \dfrac{\partial^3}{\partial r \partial \varphi \partial \cos\psi} + \\[2mm]
\dfrac{\partial^3}{\partial \varphi \partial (\cos\psi)^2} + \dfrac{\partial^3}{\partial r \partial (\cos\psi)^2} + \dfrac{\partial^3}{\partial r \partial \varphi^2} + \\[2mm]
\dfrac{\partial^3}{\partial \varphi^2 \partial \cos\psi} + \dfrac{\partial^3}{\partial r^2 \partial \cos\psi} + \dfrac{\partial^3}{\partial r^2 \partial \varphi}
\end{array}
\right) f_{\{l,m,n\}} \quad (A6)
$$

with $f_{\{i,j,k\}} \equiv S_i(r) P_j(\varphi) S_k(\cos\psi)$.

[55] Now the solution is found by solving the set of linear equations produced by the minimization

$$
\delta(\chi^2 + \lambda P) = 0 \quad (A7)
$$

The parameter $\lambda$ sets the balance between fitting the data and smoothness.

[56] *Wahba* [1990] proposes a method of generalized cross validation for choosing $\lambda$, but the conditions for its use are not satisfied in this case. Therefore a method suggested by *Press et al.* [1992] has been tested and found to work. After solving for the expansion coefficients $a_{i,j,k}$ for a particular $\lambda$, the value of $\chi^2$ is determined. The value of $\lambda$ is adjusted until $\chi^2 = 1$. The rationale for this approach is that it allows the extraction of the statistically significant information in the data. There is however the ambiguity produced by the fact that, due to the imposition of the additional restrictions on the expansion amplitudes by the penalty function, the number of independent variables being used to fit the data is not well-defined.

[57] In order to estimate the statistical uncertainties in the intensity obtained from this process [*Ramsay and Silverman*,

2006], the solutions of the linear equations resulting from the minimization are written in the form

$$
a_i = \sum_{\alpha}^{N_{pixels}} A_{i,\alpha} d_\alpha \quad (A8)
$$

where

$$
A_{i,\alpha} = \sum_j \left( D^\dagger \frac{1}{\sigma^2} D + \lambda P \right)^{-1}_{i,j} D^\dagger_{j,\alpha} \frac{1}{\sigma_\alpha^2} \quad (A9)
$$

and the superscript dagger denotes the transpose of the matrix. The variances of the expansion coefficients, $a_i$, are then

$$
Var(a_i) = \sum_{\alpha}^{N_{pixels}} A_{i,\alpha} \frac{1}{\sigma_\alpha^2} A^\dagger_{\alpha,i} \quad (A10)
$$

The variance in the intensity at point $r_p$, $\phi_p$, $cos\psi_p$ is given by the expression

$$
Var\left( I\left( r_p, \varphi_p, \cos\psi \right) \right)
$$
$$
= \sum_{i,j,k} \left( S_i(r_p) P_j(\varphi_p) S_k\left( \cos\psi_p \right) \right)^2 Var(a_{i,j,k}) \quad (A11)
$$

Multiplying equation (A11) by 1 gives a 68% confidence level and by 2 a 95% confidence level of $\pm$ the variance.

[58] The generality of the expansion functions allows for solutions in which the ion intensity is negative. A positivity constraint is an inequality not a linear operation, so it cannot be imposed directly as a constraint in the variational calculation to determine the expansion coefficients for the ion intensity. Instead, once the $\lambda$ that gives $\chi^2 = 1$ is found the resulting intensity is checked to see if there are any negative values. If so, the largest is found, and the intensity at this point, i.e., a specific $r$, $\phi$ and $\cos\psi$, is forced to zero, and a new solution for the expansion coefficients is found. This tends to remove other nearby negative intensity values. This process is repeated until there are no more negative points or until the value of $\chi^2$ increases more than 10%. The rationale is the solution of the set of linear equations is equivalent to a parameter search in a multidimensional space. To bring the solution back into the region of this space in which the intensity is positive definite, the solution would have to pass from the region in which a point is negative through the point where the intensity is zero. This process was suggested by *Wahba* [1980]. In the results shown in this paper, the resulting intensity occasionally dips slightly negative, i.e., the absolute value of minimum negative intensity is at least a factor of 100 less that maximum intensity. This occurs in regions where the ion intensity is low and the data does not sufficiently constrain the solution.

## A2. Physics

[59] There is more than just mathematics involved in deconvolving ion intensities from ENA images. As explained above, six-dimensional points in phase space are reduced to two spatial variables and the pitch angle by fixing the energy, by assuming gyrotropic symmetry and conservation of the

first adiabatic invariant, and by mapping along field lines to the equator. This requires a magnetic field model. In strong storms the field is non-dipolar [*Tsyganenko et al.*, 2003] so the *Tsyganenko and Sitnov* [2005] model is used here.

[60] The required energy-dependent charge exchange cross sections, i.e., protons with neutral hydrogen and neutral oxygen, are taken from *Barnett* [1990], *Gruntman* [1997], and *Lindsay* and *Stebbings* [2005]. Since ion distributions are deconvolved for one energy or energy-range at a time, the charge exchange cross section appears as a multiplicative factor.

[61] The emissions from charge exchange of the trapped protons with cold neutral hydrogen in the geocorona are treated as optically thin so a model of the geocorona is needed. Inside 3.5 $R_E$, the geocoronal hydrogen number density is taken to be spherically symmetric with the radial profile given by the Chamberlain model [*Chamberlain*, 1963]. An MLT dependent part [*Østgaard et al.*, 2003] is employed outside. The enhanced geocoronal hydrogen on the night side in this model was found in some cases to improve the results of ENA inversions [*Brandt et al.*, 2002]. *Zoennchen et al.* [2011] have developed a model of the hydrogen geocorona based on data from the TWINS LAD instrument during solar minimum. Results from the use of this model will be investigated in future work.

[62] There is a second source of ENAs due to charge exchange of the trapped ions with neutral oxygen in the Earth's ionosphere, i.e., the so-called low altitude emissions (LAE). The importance of the LAE and the difficulty in modeling these emissions was first pointed out by *Roelof* [1997]. Because of the high density of the cold ionospheric neutrals, the escaping ENAs have undergone multiple charge exchange interactions. Accurate calculations of the LAE intensity requires the solution of a complicated transport problem [*Bazell et al.*, 2010]. Because the LAEs are often the brightest pixels in the ENA images presented here, it is important to treat, at least approximately, the emission in these pixels. Nevertheless, these bright pixels are only a small fraction of the total number of pixels, so it has been found that an approximate treatment is adequate to obtain accurate ion distributions from the ENA images. Thus, a thick target approximation developed by *Bazell et al.* [2010] and validated by comparison with DMSP precipitation data is used. When pixel lines-of-sight intersect the Earth's ionosphere, the emission is treated as if it were from a thick target in which the ion has undergone many charge exchange interactions back and forth from charged to neutral. The point of intersection at 600 km is mapped to the equator, and the ENA intensity of the neutrals reaching pixels whose line-of-sight volume hits the ionosphere is reduced by dividing by $1 + 0.192*E^{0.551}$, where $E$ is the energy of the ion in keV [*Bazell et al.*, 2010]. This contribution is added to ENAs produced in these pixels at higher altitude by charge exchange with the geocorona.

## Appendix B: Determining Energy Spectra From Deconvolved Images

[63] In order to have energetic neutral atom images from which a valid deconvolution of the image can be performed to obtain ion distributions using the approach described in Appendix A, it is necessary that the estimated uncertainties in the pixel intensities not be too large. This means that if we recall that the deconvolution technique seeks $\chi^2 = 1$, where

$$\chi^2 \equiv \frac{1}{N_{pixels}} \sum_{\alpha}^{N_{pixels}} \left( \frac{d_\alpha - c_\alpha}{\sigma_\alpha} \right)^2 \tag{B1}$$

with the $d_\alpha$ the data in pixel $\alpha$ and the $c_\alpha$ the corresponding calculated value. If the $\sigma_\alpha$ values are so large that the maximum $\chi^2$ defined as having $c_\alpha = 0$ is already near unity, the deconvolution will not yield a meaningful ion distribution. In other words, if the uncertainties in the data are too large, there is little or no information content in the data. To ensure that there are adequate statistics in the ENA images, those used in this study have energy bands as wide as the central energy, i.e., an image for energy $E_c$ is integrated over an energy range from $E_c - \Delta E_c$ to $E_c + \Delta E_c$ with $\Delta E_c = \frac{E_c}{2}$. For high energies, this can have a significant affect as illustrated below.

[64] In order to avoid making a priori assumptions about the shape of the ion energy spectrum, the deconvolutions are done as if the measurements were made at a single energy. Thus at a fixed location at the equator, the deconvolved intensity averaged over pitch angle for energy $E_c$, $I_c$, can be written,

$$I_c = \frac{1}{\sigma_{ex} 2\Delta E_c} \int_{E_c - \Delta E_c}^{E_c + \Delta E_c} \sigma_{ex}(E) I_{phys}(E) dE \tag{B2}$$

where $\sigma_{ex}$ is the charge exchange cross section for energetic protons on neutral hydrogen. The $I_{phys}$ is the physical intensity spectrum that we seek. To extract the unknown $I_{phys}$ from under the integral sign, we expand it in terms of a set of basis functions, cubic B-splines in this study, so that

$$I_{phys} = \sum_{i=1}^{N_d} a_i S_i(E). \tag{B3}$$

[65] A set of deconvolved intensities at a series of energies, in this case the *measured* quantities, form a vector and can be expressed in matrix notation by the equation

$$\vec{I}_c = \sum_{i=1}^{N_d} \overleftrightarrow{D_{c,i}} \vec{a_i} \tag{B4}$$

where the design matrix $D_{c,i}$ is defined as

$$\overleftrightarrow{D_{c,i}} = \frac{1}{\sigma_{ex} 2\Delta E_c} \int_{E_c - \Delta E_c}^{E_c + \Delta E_c} \sigma_{ex}(E) S_i(E) dE. \tag{B5}$$

[66] There are a number of approaches that could be used to solve this set of linear equations and determine the unknown expansion coefficients, i.e., the $a_i$ values. We choose to use singular valued decomposition because it addresses the problem of the design matrix being nearly singular when there is large overlap among the energy bands that determine the $I_c$
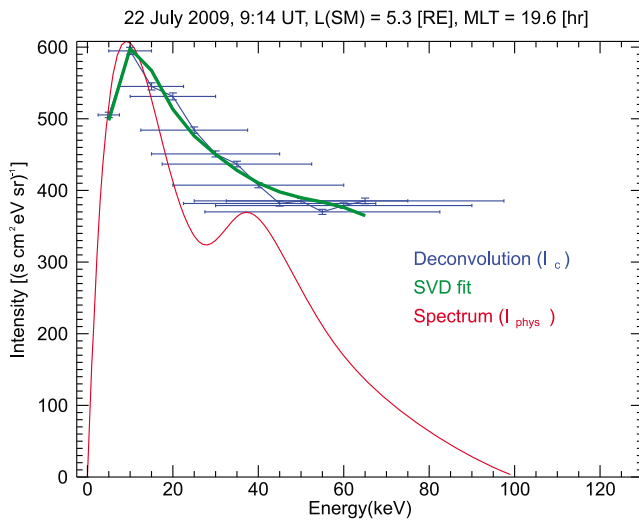
**Figure B1.** An example of the comparison between the SVD fit (green) and the deconvolution results (blue) when 4 singular values are kept. The resulting spectrum (red) is also shown.

wide energy bands. The red curve is the physical energy spectrum obtained when the 4 largest of the 13 singular values are kept. The green curve is the fit to the *data* (blue points), i.e., the result achieved when the red line is $I_{phys}(E)$. The criterion was to keep all singular values that are greater than 1/10 of the largest. The red curve is the physical energy spectrum that produces the SVD fit, i.e., the green curve, when integrated and properly weighted with the energy dependent charge exchange cross section. As is to be expected, the physical spectrum and the one obtained directly from the deconvolution of the ENA images is not affected strongly at lower energies where the charge exchange cross section and ion intensity do not vary as much over the energy bands. But at higher energies, the difference between the blue and red curves is significant. Nevertheless, both curves show the qualitative feature of a high energy tail on the distribution.

values, and it yields a solution that is the best in the least squared sense [*Press et al.*, 1992]. In the implementation of the singular value decomposition method, the design matrix is decomposed into 3 parts,

$$\overleftrightarrow{D} = \overleftrightarrow{U} \cdot \overleftrightarrow{w} \cdot \overleftrightarrow{V^T} \qquad (B6)$$

where $\vec{U} \, and \, \overleftrightarrow{V^T}$ (the superscript $T$ denotes the transpose) are orthogonal matrices and $\overleftrightarrow{w}$ is a diagonal matrix containing the singular values. The solution to the equation for the unknown expansion coefficients is then

$$\vec{a} = \overleftrightarrow{V} \cdot \frac{1}{\overleftrightarrow{w}} \cdot \overleftrightarrow{U^T} \cdot \vec{I_c} \qquad (B7)$$

since the inverse of an orthogonal matrix is just the transpose and the inverse of a diagonal matrix is another diagonal matrix containing the inverse of the original diagonal elements. The smaller values of the singular values are then omitted from the product because their omission increases $\chi^2$, and they represent linear combinations which are most sensitive to uncertainties in the data. The result is a solution for the vector $\vec{a}$, the coefficients that give $I_{phys}(E)$, the desired physical spectrum.

[67] To illustrate the method, we will use the deconvolved solutions on 22 July 2009 at 0914UT for the energies, 5–65 keV in steps of 5 keV as the *data*. Thus there are 13 data points, and the energy integrals extend from 2.5–97.5 keV. We choose the location of THEMIS d at this time because we compare the results of this calculation with the in situ measurements of THEMIS d. For this case, we chose 14 splines equally spaced from 0.0 to 100 keV. The initial spline amplitude was set to 0 to ensure that the intensity went to 0 at 0.0 keV. The results are shown in Figure B1. The blue points are the intensities obtained directly from the deconvolution of the ENA images at the location and time shown at the top of the plot. The horizontal bars illustrate the overlap of the

## References

Angelopoulos, V. (2008), The THEMIS mission, *Space Sci. Rev.*, *141*(1–4), 5–34, doi:10.1007/s11214-008-9336-1.

Barnett, C. F. (1990), Atomic data for fusion, volume 1: Collisions of H, H$_2$, He, and Li atoms and ions with atoms and molecules, *Tech. Rep., ORNL-6086/V1*, Oak Ridge Natl. Lab., Oak Ridge, Tenn.

Bazell, D., E. C. Roelof, T. Sotirelis, P. C. Brandt, H. Nair, P. Valek, J. Goldstein, and D. McComas (2010), Comparison of TWINS images of low-altitude emission of energetic neutral atoms with DMSP precipitating ion fluxes, *J. Geophys. Res.*, *115*, A10204, doi:10.1029/2010JA015644.

Brandt, P. C., S. Ohtani, D. G. Mitchell, M.-C. Fok, E. C. Roelof, and R. Demajistre (2002), Global ENA observations of the storm mainphase ring current: Implications for skewed electric fields in the inner magnetosphere, *Geophys. Res. Lett.*, *29*(20), 1954, doi:10.1029/2002GL015160.

Burch, J. L. (2000), Image mission overview, *Space Sci. Rev.*, *91*, 1–14, doi:10.1023/A:1005245323115.

Chamberlain, J. W. (1963), Planetary coronae and atmospheric evaporation, *Planet. Space Sci.*, *11*, 901–960, doi:10.1016/0032-0633(63)90122-3.

deBoor, C. (1978), *A Practical Guide to Splines*, Springer, New York, doi:10.1007/978-1-4612-6333-3.

Farris, M. H., and C. T. Russell (1994), Determining the standoff distance of the bow shock: Mach number dependence and use of models, *J. Geophys. Res.*, *99*, 17,681–17,689, doi:10.1029/94JA01020.

Grimes, E. W., J. D. Perez, J. Goldstein, D. J. McComas, and P. Valek (2010), Global observations of ring current dynamics during corotating interaction region–driven geomagnetic storms in 2008, *J. Geophys. Res.*, *115*, A11207, doi:10.1029/2010JA015409.

Gruntman, M. (1997), Energetic neutral atom imaging of space plasmas, *Rev. Sci. Instrum.*, *68*, 3617–3656, doi:10.1063/1.1148389.

Kistler, L. M., F. M. Ipavich, D. C. Hamilton, and G. Gloeckler (1989), Energy spectra of the major ion species in the ring current during geomagnetic storms, *J. Geophys. Res.*, *94*, 3579–3599, doi:10.1029/JA094iA04p03579.

Krieger, A. S., A. F. Timothy, and E. C. Roelof (1973), A coronal hole and its identification as the source of a high velocity solar wind stream, *Sol. Phys.*, *29*, 505–525, doi:10.1007/BF00150828.

Lindsay, B. G., and R. F. Stebbings (2005), Charge transfer cross sections for energetic neutral atom data analysis, *J. Geophys. Res.*, *110*, A12213, doi:10.1029/2005JA011298.

McComas, D. J., H. O. Funsten, and E. E. Scime (1998), Advances in low energy neutral atom imaging, in *Measurement Techniques in Space Plasmas-Fields*, *Geophys. Monogr. Ser.*, vol. 103, edited by R. F. Pfaff, J. E. Borovsky, and D. T. Young, pp. 275–280, AGU, Washington, D. C.

McComas, D. J., et al. (2009a), The Two Wide-angle Imaging Neutral-atom Spectrometers (TWINS) NASA Mission-of-Opportunity, *Space Sci. Rev.*, *142*, 157–231, doi:10.1007/s11214-008-9467-4.

McComas, D. J., et al. (2009b), Global observations of the interstellar interaction from the Interstellar Boundary Explorer (IBEX), *Science*, *326*(5955), 959–962, doi:10.1126/science.1180906.

McComas, D. J., N. Buzulukova, M. G. Connors, M. A. Dayeh, J. Goldstein, H. O. Funsten, S. Fuselier, N. A. Schwadron, and P. Valek (2012), TWINS and IBEX ENA imaging of the 5 April 2010 substorm, *J. Geophys. Res.*, *117*, A03225, doi:10.1029/2011JA017273.

McFadden, J. P., C. W. Carlson, D. Larson, M. Ludlam, R. Abiad, B. Elliot, P. Turin, M. Marckwordt, and V. Angelopoulos (2008), The THEMIS ESA Plasma Instrument and In-flight Calibration, *Space Sci. Rev.*, *141*, 277–302, doi:10.1007/s11214-008-9440-2.

Mitchell, D. G., et al. (2000), High energy neutral atom (HENA) imager for the Image mission, *Space Sci. Rev.*, *91*, 67–112, doi:10.1023/A:1005207308094.

Mitchell, D. G., P. C. Brandt, E. C. Roelof, D. C. Hamilton, K. D. Retterer, and S. Mende (2003), Global imaging of O$^+$ from IMAGE/HENA, *Space Sci. Rev.*, *109*, 63–75, doi:10.1023/B:SPAC.0000007513.55076.00.

Ohtani, S., P. C. Brandt, D. G. Mitchell, H. Singer, M. Nosé, G. D. Reeves, and S. B. Mende (2005), Storm-substorm relationship: Variations of the hydrogen and oxygen energetic neutral atom intensities during storm-time substorms, *J. Geophys. Res.*, *110*, A07219, doi:10.1029/2004JA010954.

Østgaard, N., S. B. Mende, H. U. Frey, G. R. Gladstone, and H. Lauche (2003), Neutral hydrogen density profiles derived from geocoronal imaging, *J. Geophys. Res.*, *108*(A7), 1300, doi:10.1029/2002JA009749.

Perez, J. D., G. Kozlowski, P. C. Brandt, D. G. Mitchel, J.-M. Jahn, C. J. Pollock, and X. X. Zhang (2001), Initial ion equatorial pitch angle distributions from medium and high energy neutral atom images obtained by IMAGE, *Geophys. Res. Lett.*, *28*, 1155–1158, doi:10.1029/2000GL012636.

Pollock, C. J., et al. (2000), Medium energy neutral atom (MENA) imager for the IMAGE mission, *Space Sci. Rev.*, *91*, 113–154, doi:10.1023/A:1005259324933.

Press, W. H., S. A. Teukolsky, W. T. Vettering, and B. P. Flannery (1992), *Numerical Recipes*, Cambridge Univ. Press, Cambridge, U. K.

Ramsay, J. O., and B. W. Silverman (2006), *Functional Data Analysis*, 2nd ed., Springer, New York.

Roelof, E. C. (1997), ENA emission from nearly mirroring magnetospheric ions interacting with the exosphere, *Adv. Space Res.*, *20*, 361–366.

Shue, J.-H., J. K. Chao, H. C. Fu, C. T. Russell, P. Song, K. K. Khurana, and H. J. Singer (1997), A new functional form to study the solar wind control of the magnetopause size and shape, *J. Geophys. Res.*, *102*, 9497–9511.

Tsurutani, B. T., W. D. Gonzalez, A. L. C. Gonzalez, F. Tang, J. K. Arballo, and M. Okada (2006), Corotating solar wind streams and recurrent geomagnetic activity: A review, *J. Geophys. Res.*, *111*, A07S01, doi:10.1029/2005JA011273.

Tsyganenko, N. A., and M. I. Sitnov (2005), Modeling the dynamics of the inner magnetosphere during strong geomagnetic storms, *J. Geophys. Res.*, *110*, A03208, doi:10.1029/2004JA010798.

Tsyganenko, N. A., H. J. Singer, and J. C. Kasper (2003), Storm-time distortion of the inner magnetosphere: How severe can it get?, *J. Geophys. Res.*, *108*(A5), 1209, doi:10.1029/2002JA009808.

Turner, N. E., E. J. Mitchell, D. J. Knipp, and B. A. Emery (2006), Energetics of magnetic storms driven by corotating interaction regions: A study of geoeffectiveness, in *Recurrent Magnetic Storms: Corotating Solar Wind Streams*, *Geophys. Monogr. Ser.*, vol. 167, edited by B. Tsurutani et al., pp. 113–124, AGU, Washington, D. C., doi:10.1029/167GM11.

Valek, P., P. C. Brandt, N. Buzulukova, M.-C. Fok, J. Goldstein, D. J. McComas, J. D. Perez, E. Roelof, and R. Skoug (2010), Evolution of low-altitude and ring current ENA emissions from a moderate magnetospheric storm: Continuous and simultaneous TWINS observations, *J. Geophys. Res.*, *115*, A11209, doi:10.1029/2010JA015429.

Vallat, C., et al. (2004), First comparisons of local ion measurements in the inner magnetosphere with energetic neutral atom magnetospheric image inversions: Cluster-CIS and IMAGE-HENA observations, *J. Geophys. Res.*, *109*, A04213, doi:10.1029/2003JA010224.

Wahba, G. (1980), Ill posed problems: Numerical and statistical methods for mildly, moderately and severely ill posed problems with noisy data, *Tech. Rep., 595*, Univ. of Wisc.–Madison, Madison.

Wahba, G. (1990), *Spline Models for Observational Data*, Soc. for Ind. and Appl. Math., Philadelphia, Pa., doi:10.1137/1.9781611970128.

Zoennchen, J. H., J. J. Bailey, U. Nass, M. Gruntman, H. J. Fahr, and J. Goldstein (2011), The TWINS exospheric neutral H-density distribution under solar minimum conditions, *Ann. Geophys.*, *29*, 2211–2217, doi:10.5194/angeo-29-2211-2011.